Optical and Quantum Electronics (2023) 55:290
https://doi.org/10.1007/s11082-023-04551-z

Ultra high resolution point spread function based on photonic crystal lens for 3D biomedical applications

Norhan A. Salama[1,3] · Mohamed A. Swillam[2] · Mohamed Farhat O. Hameed[3,4,5] · Y. Badr[6] · Shaimaa M. Alexeree[1] · Salah S. A. Obayya[3,7]

Received: 3 October 2022 / Accepted: 3 January 2023 / Published online: 4 February 2023
© The Author(s) 2023

Abstract
In this paper, a novel design of superlens based on photonic bandgap structure for high resolution point spread function (PSF) is reported at a wavelength of 3 μm. The lens is able to generate a non-diffraction Bessel beam with a number of focusing points with variant resolution limits. The optimized structure provides high resolution in both lateral and axial directions. The maximum achieved lateral resolution of PSF is down to ~ 0.27λ with corresponding axial resolution down to ~ 0.57λ attaining a FOM, the inverse of the product of both resolution limits, of ~ 6.49. Meanwhile, the maximum axial resolution is down to ~ 0.4λ with corresponding lateral resolution down to ~ 0.33λ with a FOM of ~ 7.34. In addition, the proposed design is able to generate a focusing point extended in space up to ~ 0.98 μm with a sub-diffraction lateral resolution down to ~ 0.47λ. Furthermore, the reported superlens demonstrates a sub-diffraction focusing in lateral direction along the range the bandgap wavelengths (from 2.4 to 3.6 μm) showing a significant increase of focal depth when decreasing the operating wavelength. Remarkably, a high focal depth up to ~ 1.77 μm is achieved at the operating wavelength of 2.6 μm. The suggested design has a tremendous potential in 3D biological imaging and biosensing applications.

Keywords Metalens · Point spread function · Sub-diffraction focusing · Lateral and axial light confinement · 3D imaging · Superlens

1 Introduction

The resolution of conventional optical systems is constrained by the diffraction limit where the achievable imaging resolution is limited in both the lateral and axial directions to half of the incident wavelength (λ/2) and to the incident wavelength (λ), respectively, termed as Abb's diffraction limit (Rayleigh 1879). Despite most of the technological advancements in super resolution imaging beating the diffraction limit in lateral direction, major challenges have been imposed for 3D position localization. The 3D localization is crucial to investigate the biological structures in depth and the dynamics of the freely moving particles in

✉ Salah S. A. Obayya
sobayya@zewailcity.edu.eg

Extended author information available on the last page of the article

3D volume. The lateral and axial light confinement of the so called point spread function (PSF) (Kihm 2011) plays the key role for resolving the subcellular fine features against their neighboring background in 3D space. In other word, the gradient of the electromagnetic field either in lateral or axial dimension of PSF allows the fine discrimination between two points in each dimension. Unfortunately, the intrinsic tradeoff between the lateral and axial light confinement is inevitable and results in the deterioration of the retrieved optical image in 3D space. Different techniques have been introduced to overcome the PSF diffraction limit. For instance, confocal laser scanning microscopy (CLSM) (Kihm 2011) and the stimulated emission depletion (STED) microscopy offer spatial high resolution PSF down to nanometer scale (Willig et al. 2006). However, the high densely focused illumination scanning point and the use of the fluorescent dyes may cause photodamage, photobleaching or cytotoxicity of the living cell. Other techniques based on generating structured interference at a focal spot such as 4Pi microscopy (Hell et al. 1994; Sandeau and Giovannini 2006), I^5M microscopy (Gustafsson et al. 1999), the mirror-enhanced axial resolution technique (Yang et al. 2016) and standing-wave excitation microscopy (Bailey et al. 1993) have been reported excluding the need for high illumination or using fluorescent dyes. The 4Pi microscopy, as an example, provides a resolution limit of PSF down to 75 nm in axial direction and down to 113 nm in lateral direction (Sandeau and Giovannini 2006). For I^5M microscopy, it has been proven to provide an axial resolution down to 100 nm (Gustafsson et al. 1999). The mirror-enhanced axial resolution technique allows axial resolution limit down to 110 nm and lateral resolution limit down to 19 nm (Yang et al. 2016). Although the aforementioned techniques have tremendous impact for beating the diffraction limit of PSF in both lateral and axial directions, they suffer from the drawbacks of the complexity of the system alignment that hinder them from practical application certainly for non-experts.

On the other hand, engineered superlenses based on photonic crystal (PhC), metamaterial (MM) and metalens (ML) have been extensively reported for overcoming the diffraction limit with a strong potential to replace the conventional lenses in optical systems. Photonic crystal and MM unique features unveiled an impressive assemblage of a number of applications such as imaging (Cui et al. 2014), biosensing (Zhuo and Cunningham 2015), photocatalysis (Zhang and John 2021), light coupling (Areed et al. 2018), digital coding (Cui et al. 2014) (Mohammadi et al. 2022), multiplexer/ demultiplexer (Zheng et al. 2010; Pan et al. 2021). Imaging is at the forefront of these applications utilizing diverse fundamental mechanisms (Padilla and Averitt 2022). However, most of the reported studies based on superlens concerned only the diffraction limit in lateral dimension while the light confinement in the axial dimension remained elusive. Hyperbolic metamaterial (HMM) is the cutting edge technology overcoming the diffraction limit in lateral direction in near and far-fields (Salama et al. 2020; Salama et al. 2019; Salama ailed 2018; Jacob et al. 2006). HMM, an extreme anisotropic structures capable of coupling to the evanescent high wave vectors in air that carry the subwavelength features to propagating modes inside and in the near field of HMM demonstrating a negative refraction behavior. Hence, the propagating modes can be manipulated for subwavelength focusing realization. Recently, HMM based on intrinsic InAs/doped InAS has been introduced beating the diffraction limit along MID IR range reaching down to 0.19λ and extended in space up to 3.2 μm for $\lambda = 7.6$ μm. However, the axial localization of the image is hindered by the exponentially decaying evanescent waves. Metasurfaces, a sub wavelength 2D structures where light manipulation is achievable by introducing phase discontinuity across the surface, is an alternative approach tackling different imaging constrains. The aberration free, non-diffracted Bessel beam and the focal depth have been addressed based on metasurfaces (Berry and Balazs 1979; Ren,

et al. 2021; Aieta et al. 2012; Fan et al. 2020). However, the axial light confinement of PSF is merely introduced except for few efforts -such as hydrogenated amorphous Si nanodiscs metasurface providing minor lateral light confinement (Lee et al. 2019). MID IR imaging has a tremendous impact for biological applications. Since, the standard building blocks of biological samples such as proteins, lipids, nucleic acids have distinctive IR spectra (Miller and Dumas 2006). In addition, IR radiation is non-ionizing and hence no altering in the cell composition even if probed for a coarse of time. Despite the developments of IR microscopy, the serious constrains are imposed from the poor spatial resolution that reaches down to (~0.77λ) (Carr 2001; Silien et al. 2012). Silicon photonic crystal finds the potential for MID IR application devices providing the advantages of the ease of fabrication and CMOS compatibility (Shankar et al. 2011). Silicon photonic crystals (Si-PhC) holds true the applicability of self-imaging and multimode interference in numerous studies (Zhang et al. 2006; Shaari and Azliza 2010). Photonic crystal (PhC) is a periodic array of dielectric material, hence periodic refractive indices in one, two or three dimensions in space (Joanopoulos 2008; Banaei et al. 2015). The photonic bandgap, the spectral range at which the propagation of the electromagnetic waves is forbidden in a certain direction, is representing the key feature of the PhC. The PhC has the advantages of the scalability, large photonic bandgap (PBG), slow light mode, and self-collimation (Joanopoulos 2008). The advantages of PhC open the gate for tremendous applications such as 2-to1 digital multiplexing with small area, fast response and high contrast ratio (Maleki and Soroosh 2022), optical demultiplexing with high transmission efficiency in multiple channels (Mohammadi et al. 2019), logic gates with high power difference in the high and low logic modes (Parandin and Malmir 2020), decoders with small size and enhanced delay time (Maleki et al., 2020, 2019b; Maleki and Soroosh 2020), encoder with controllable transmission through the waveguides (Haddadan et al. 2020), analog to digital converters supporting high sampling rates (Mehdizadeh et al. 2017), ultra-fast and compact all-optical RS flip-flop (Zamanian-Dehkordi et al. 2018; Abbasi et al. 2011), and an ultra-fast all-optical full adder (Notomi 2008; Shinya et al. 2006; Malei 2020).

In this paper, we report a sub-diffraction PSF in both lateral and axial directions based on Si-PhC band gap metalens structure. We utilize the capability of (Si-PhC) to provide a multimode interference phenomenon in MID IR for creating hot spots/focusing points of electric field within the cavity with sub-diffraction limit in lateral and axial directions reaching down to (~0.27λ) and (~0.42λ), respectively. Worthwhile, the inevitable challenge of obtaining simultaneous sub-diffraction focusing in both directions using a simple meta-lens design has been addressed attaining resolution limits comparable to the recent reported studies concerning each direction separately. For instance, a recent study of sub-diffraction focusing in lateral direction using HMM demonstrates a resolution limit down to (~0.2λ) (Salama et al. 2020). Another study based on meta-surface design has presented an axial focusing resolution down to (~0.41λ) (Lee et al. 2019). In addition, the proposed design not only provides a number of focusing points inside the cavity but an extended focusing point outside the lens with manipulated focal depth reaching up to (~0.98 μm) as well. Moreover, the structure demonstrates focusing behavior with high focal depth when the operating wavelength is blue shifted attaining its maximum focal depth (~1.78 μm) at operating wavelength of 2.6 μm.

The paper is organized as follows: First, we demonstrate the cavity design stages for obtaining multimode interference (MMI) at operating wavelength of 3 μm. Second, the raised hot spots/focusing points resolution are enhanced through adding metallic inclusions, silver rods then silver slit. Third, the silver slit parameters are optimized providing significant enhancement of lateral and axial focusing resolution, high FOM and high focal

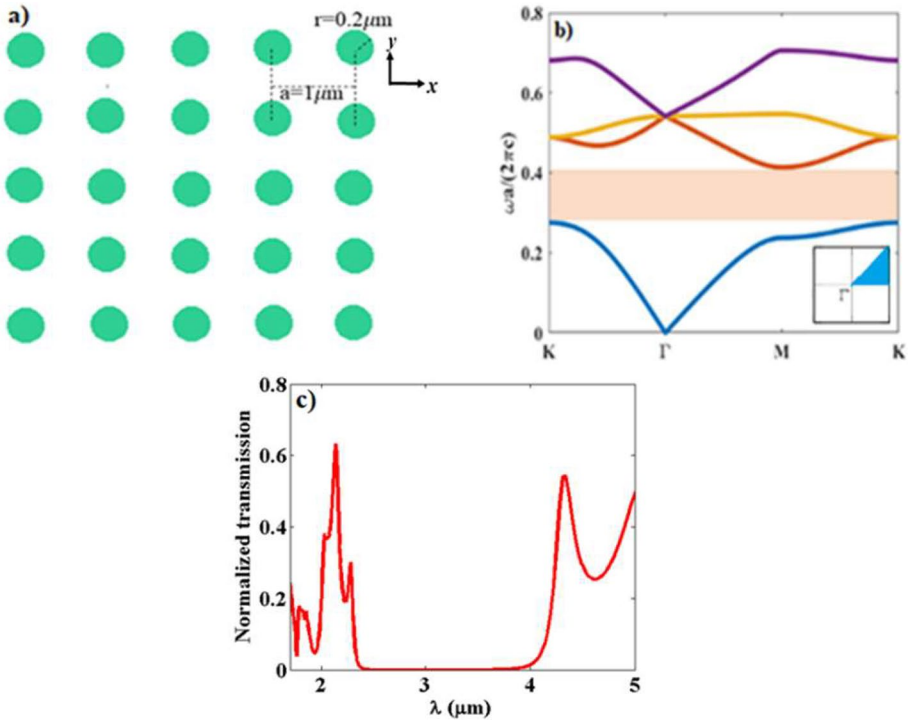

Fig. 1 **a** A schematic of the PhC structure based on square lattice of Si pillars of radius r = 0.2 μm and lattice constant a = 1 μm. **b** A demonstration of TE band diagram of the PhC lattice. **c** The normalized transmission spectrum of TE mode

depth. Finally, we report the metalens performance along the range of the band gap wavelengths demonstrating the ability to extend the focal depth in free space by blue shift of the working wavelength.

2 Design considerations of the proposed meta-lens

The proposed meta-lens design is based on a square lattice of Si pillars with dielectric permittivity (ε = 12.5), radius r = 0.2 μm and the lattice constant a = 1 μm as may be noted from Fig. 1a. The structure consists of 25 pillars in *x*-direction and in 16 pillars in *y*- direction. As the studied structure represents an ideal 2D PhC, the height of the rods is assumed to be sufficiently large, multiple of the propagating wavelength, whereas no light cone exists and the PBG is fully determined by the modes in the Brillouin zone near special point K in the lower band and M in the higher band representing the extrema in their respective bands (Jin et al. 2012).

To calculate the propagating Eigen modes of the structure, two dimensional Plane Wave Expansion method (PWE) (Johnson and Joannopoulos 2001) is applied for a single unit cell of (r/a = 0.2) using periodic boundary conditions in x and y directions. The band diagram of the transverse electric (TE) mode is presented in Fig. 1b showing a bandgap formation in the range from 2.4 to 3.6 μm. The band diagram demonstrates

good agreement with the band diagram in reference (Zhang et al. 2006; Ibrahim et al. 2021). The bandgap formation is verified by examining the transmission spectrum using Finite element method with scattering boundary conditions for 5 × 5 unit cells as shown in Fig. 1c. The obtained transmission spectrum is in analogy with the transmission spectrum of the same unit cell structure with dimensions of (r/a = 0.225) presented in ref Ibrahim et al. (2021). The bandgap formation is verified by examining the transmission spectrum using Finite element method with scattering boundary conditions for 5 × 5 unit cells as shown in Fig. 1c. The obtained transmission spectrum is in analogy with the transmission spectrum of the same unit cell structure with dimensions of (r/a = 0.225) presented in ref Ibrahim et al. (2021). The transverse magnetic (TM) mode of this design doesn't provide a complete PBG, hence it is not suitable for creating guided modes. High efficient waveguide (WG) coupled cavity design is created and developed throughout the structure design for guiding the light and induce a constructive interference resulting in multimode interference forming focusing points with high resolution at the operating wavelength λ = 3 μm (the central band gap wavelength) of the TE mode. Initially, the waveguide is created by removing three arrays of Si pillars along the vertical direction of PhC forming a rectangular defect. Then, the waveguide is coupled with a terminal semi-elliptic cavity with a vertically aligned major semiaxis ($\boldsymbol{l}_2 = 7$a) centered at a distance 13a from the input side, and a horizontally aligned minor semiaxis ($\boldsymbol{l}_1$) of variant dimensions centered in the middle of x-axis, etching the bottom Si pillars if intersected with the elliptic dimensions as demonstrated in Fig. 2a–d. The design of multimode cavity is further developed by adding Ag rods at the terminal of the cavity and then, integrated with Ag slit on top of the structure. The final design allows for multiple focusing functionalities including sub-diffraction PSF, sub-diffraction focusing in axial and lateral direction, either inside or outside the lens. The calculation of the resolution limit in the lateral direction at specified focusing point is estimated at a horizontal line plane crossing the maxima of the field profile in the axial direction of this point. On the other side, the resolution limit of the axial direction of a focusing point is estimated at the vertical axial line plane of the point. The calculation of the resolution limit is determined by the full width at half maximum of the electric field profile with respect to the propagating wavelength as follows:

$$Resolution = \frac{FWHM}{\lambda} \tag{1}$$

The overall resolution limit of each PSF is evaluated by an introduced single expression of a figure of merit (FOM) which is provided by the inverse of the product of the resolution limit in both lateral and axial directions as the following:

$$FOM = \frac{1}{lateral\ resolution * Axial\ resolution} \tag{2}$$

The maximum FOM of the conventional optical systems, that obey Abb's diffraction limit, is 2. In the following study, we will demonstrate a dramatic enhancement of FOM reaching up to ~ 8.

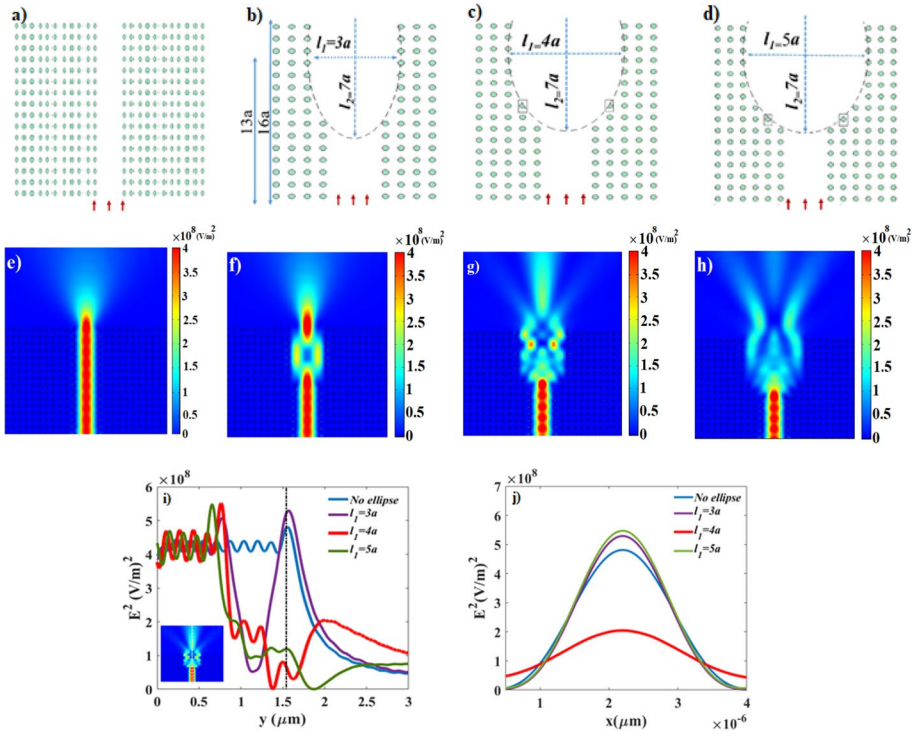

Fig. 2 Schematic representations of the creation of PhC cavity stages. **a** rectangular defect waveguide. After that, an elliptic cavity coupled to the waveguide etching the intersecting bottom Si pillars with a fixed major semiaxis ($l_2 = 7a$) and a variable minor semiaxis (l_1): **b** $l_1 = 3a$, **c** $l_1 = 4a$ and **d** $l_1 = 5a$. **e–f** The electric field intensity distributions in x–y plane for each design, respectively. **i** The electric field intensity profiles along the propagation direction at the focal plane (the dashed white line) demonstrated in the inset. The vertical dashed line represents the lens interface. **j** The electric field intensity profiles at the horizontal focal planes represented by the white dashed lines in Fig.(**e–h**)

3 Results and discussion

The electric field intensity distribution in x–y plane through the studied structures are demonstrated in Fig. 2e–h. The Finite element method (FEM) software package (Comsol Multiphysics) (https:www.comsol.com, comsol-multiphysics. 2017) has been used for simulating the optical response of the proposed design. Scattering Boundary conditions are used on all boundaries except at the input port. The input port type is rectangular propagating with transverse electric field polarization. Extremely fine meshing is used overall the simulation with maximum element size of 0.6μm and minimum element size of 1.2nm. For the accuracy of calculations of the full width at half maximum at the focusing points, we set a custom meshing at the focusing points of 10 nm. The obtained electric field profiles of the different cavity designs are in high agreement with the electric field profiles of the multimode interference patterns in the two-dimensional silicon photonic crystal waveguides with fairly difference in the ratios of (r/a) and (a/λ) presented in reference (Zhang et al. 2006). For the rectangular defect, the electric field is guided and rapidly decays outside the structure as can be noted from Fig. 2e. An elliptic cavity, created by etching Si rods, is coupled to the WG with optimized dimensions. The elliptic cavity allows the field to

propagate coherently in an angular spectrum leading to a superposition and creation of focusing points as will be explained further in the paper. A dramatic change of the EM propagation behavior is observed by varying the minor semiaxis dimensions of the ellipse. For the structure of ($l_1 = 3$a), a single focusing point is observed at the interface of the lens as shown in Fig. 2f. A unique behavior is observed for the structure of ($l_1 = 4$a) that exhibits multiple focusing points inside and outside the cavity as a result of multimode interference as shown in Fig. 2g. By increasing the semiaxis dimension to ($l_2 = 5$a), focusing points deteriorate as may be noted from Fig. 2h.

Figure 2i represents the different axial electric field intensity profiles throughout the four cases demonstrating the location of the focusing points along the axis of the designs. A significant axial electric field confinement for the structure of ($l_1 = 3$a) compared to other designs. is observed at the interface of the lens. However, the structure of ($l_1 = 4$a) provides a considerable advantage over other designs, since it allows the projection of the focal spot to a distance away from the lens interface (focal depth = 4 μm) which is of pivotal importance for imaging systems. In addition, the structure of ($l_1 = 4$a) supports a multimode interference introducing a number of focusing points inside the cavity. Figure 2j demonstrates the electric field intensity profiles at the x-line planes of the focusing points represented by white dashed lines in fig.(e–f), respectively. Based on this study, a special attention has been devoted to the structure of ($l_1 = 4$a) as a promising design for diverse focusing features. Nevertheless, the structure of ($l_1 = 4$a) suffers from the low lateral resolution limit down to (~ 0.72λ), above the diffraction limit, as illustrated by red curve in Fig. 2j. In addition, although the structure exhibits a high focal depth, the axial localization is hindered by the poor intensity gradient along the axial axis as illustrated by red curve in Fig. 2i.

Hence, the structure of ($l_1 = 4$a), denoted as PhC lens, is further developed in order to enhance the resolution of the focusing points in both lateral and axial directions highlighting the corresponding focal depth. First, two silver rods, with radius 0.2 μm, are added at the terminal of the PhC lens cavity. Further, the PhC lens is integrated with a silver slit mounted on top of the lens. The proposed design is presented in Fig. 3a. The working principle of the suggested design can be explained using the ray tracing as shown in Fig. 3b. The schematic shows that the PhC cavity that acts as a Bragg reflector and induce light interference. In particular, the carved elliptic cavity allows the light waves to propagate coherently in an angular spectrum leading to a superposition of the plane waves and results in a non-diffraction Bessel beam profile introducing focusing points with variant intensities and resolution at different locations. Figure 3c and d show the electric field intensity distributions for both structures, PhC/Ag rods and PhC/Ag rods/Ag slit. Significant entire focusing points are observed upon the modifications. The focusing resolution is examined for the focusing points located on the focal axis and denoted as P1, for the outside focusing point, and P2, for the entire focusing point, as labeled in Fig. 3c, d. At P1, the lateral resolution is enhanced from (~ 0.72λ) to (~ 0.47λ) upon the modification from the initial design to PhC/Ag rods lens. When PhC/Ag rods/Ag slit is used, the lateral resolution is enhanced to (~ 0.33 λ) as may be observed from Fig. 3e. At P2, the focusing is hardly observed for the PhC lens, while the addition of Ag rods gives rise to a prominent focusing point at P2 surrounded with a number of focusing points. Upon adding the optimized Ag slit, the lateral resolution of P2 is enhanced from (~ 0.3λ) to (~ 0.28λ) as demonstrated in Fig. 3f. On the other hand, the axial resolutions at both points are demonstrated through observing the electric field profile along the focal axis as can be noted from Fig. 3g. The axial electric field confinement for PhC lens is fair. After adding of Ag rods, a dramatic enhancement of the electric field confinement is obtained at the two points, P1 and P2, where the axial resolution reaches down to (~ 1.61λ) at P1 and down to (~ 0.43λ) at P2 beating the axial

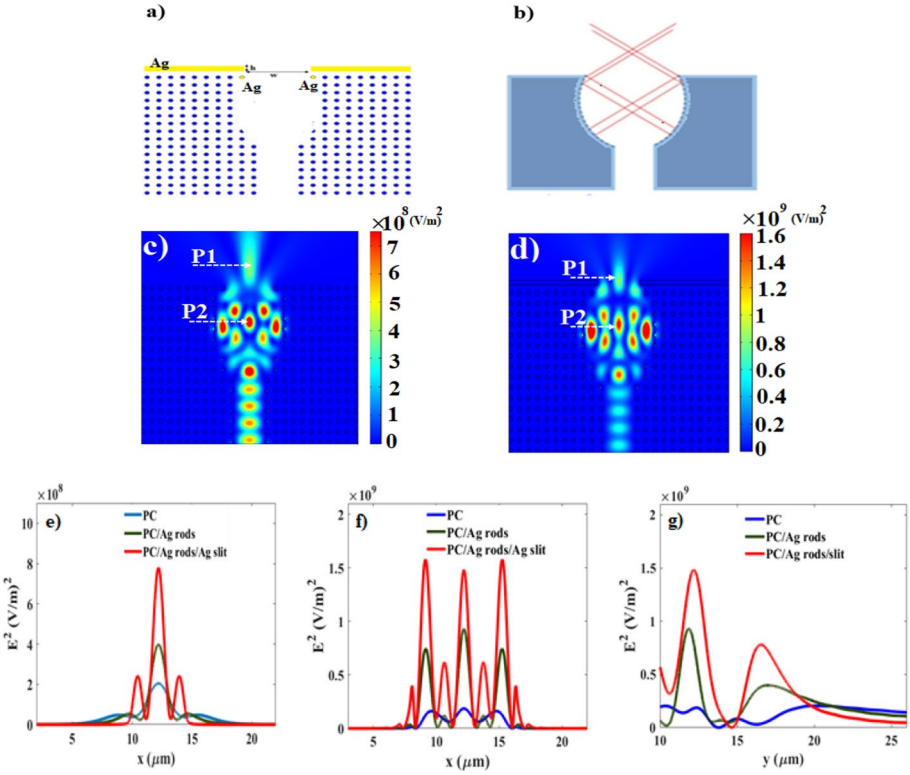

Fig. 3 **a** A schematic representation of the proposed lens design. **b** The ray tracing diagram throughout the elliptic cavity. **c**, **d** The electric field intensity distributions at operating wavelength λ = 3 μm in x–y plane of the PhC lens with and without Ag slit, respectively. **e** The Lateral electric field intensity profiles at focal planes at (P1) for PhC lens (blue), PhC lens with Ag rods (green) and PhC lens with Ag rods and slit(red). **f** The Lateral electric field intensity profiles at focal planes at (P2) for the three cases. **g** The electric field intensity profile at the axial focal planes passing through P2 and P1

diffraction limit. Further enhancement is achieved for the axial resolution at P1 upon adding Ag slit where the resolution reaches down to (~ 0.94λ), contrarily, the axial resolution at P2 is reduced down to (~ 0.47λ). Remarkably, Ag slit introduces a significant effect on focusing points features including the lateral and the axial resolution and as well the focal depth of P1.

In the next investigation, we study the effect of the Ag slit parameters on the focusing features at both points P1 and P2. First, the focusing resolution in both lateral and axial directions and their corresponding focal depth at P1 are investigated with respect to the slit thickness (*h*) with constant width (w = 5 μm) as demonstrated in Fig. 4a. Despite that the presence of slit exhibits a remarkable enhancement in lateral focusing resolution, black curve, the effect of the slit thickness is relatively limited in that direction reaching its maximum down to ~ 0.35λ at focal depth 257 nm for (h = 0.7 μm). Contrarily, the axial resolution is significantly enhanced by increasing the slit thickness reaching down to ~ 0.76λ for (*h* = 2.5 μm).

However, the axial resolution enhancement is obtained at the cost of focal depth as the focusing point is obtained inside the slit. Consequently, the FOM is increasing with

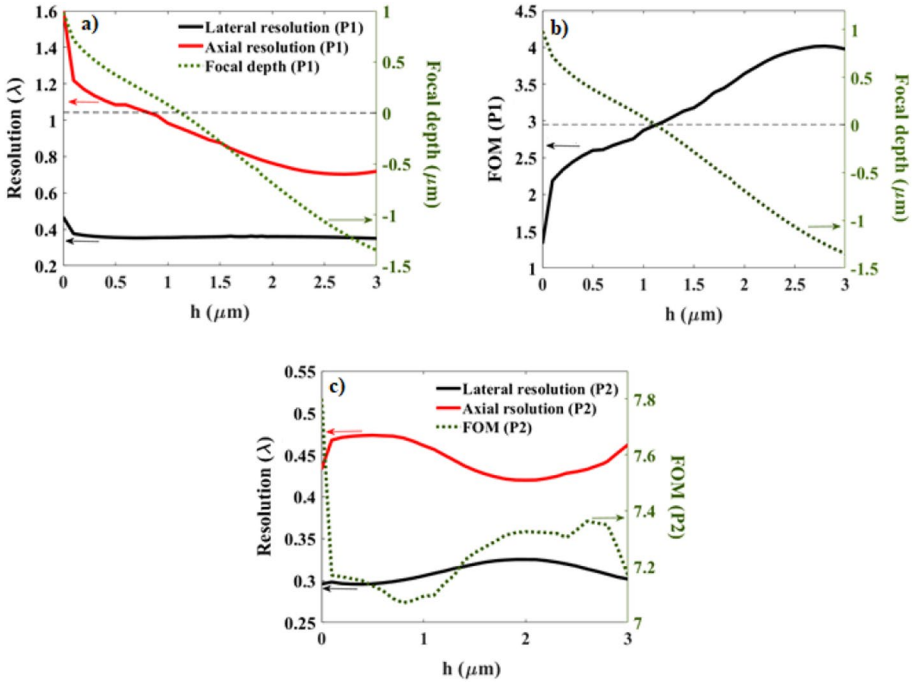

Fig. 4 **a** P1 lateral resolution (black), the corresponding axial resolution (red) and focal depth (green) against the slit thickness (h) when the slit width is fixed at w = 5 μm. **b** The evaluated FOM of P1(black) and the corresponding focal depth (green) against the slit thickness (h). The horizontal dotted line represents the lens interface. **c** P2 lateral resolution (black), the axial resolution (red) and FOM against the slit thickness (h)

increasing the slit thickness attaining its maximum (4.015) at a focal plane well below the lens interface (− 1.25 μm) for (h = 2.8 μm). The highest axial resolution achieved outside the lens is down to ~ 0.98λ, barely beating the axial diffraction limit, at 81 nm away from the lens with corresponding FOM (2.756) for (h = 0.9 μm).

A similar analysis is further performed at P2 as presented in Fig. 4c, except for the focal depth as it's not applicable in this position. In absence of Ag slit, the lens demonstrates the highest FOM (FOM = 7.802) as a result of high resolution in both directions, lateral and axial reaching down to 0.296λ and 0.433λ, respectively. The slit thickness parameter exhibits tradeoffs between the lateral and axial resolution where the lateral resolution reaches its maximum down to (0.2957λ) while the axial resolution reaches its least down to (~ 0.47λ) for (h = 0.4 μm) and vice versa, the axial resolution reaches its maximum down to (~ 0.42λ) when the lateral resolution reaches its least down to (~ 0.33λ) for (h = 2 μm).

Now, the effect of the slit width (w) is examined at constant thickness (h = 0.4 μm), at which the highest lateral resolution is obtained. Figure 5a shows the focusing resolution at P1 behavior along the range of slit widths (w = 3 to 5.1 μm). The highest lateral resolution is down to ~ 0.31λ for (w = 4.55 μm) with an axial resolution down to (~ 0.73λ) at a plane below the lens interface (− 0.302 μm). In addition, the axial resolution reaches its maximum down to 0.5802λ for (w = 4 μm), where the lateral resolution observed is down to (~ 0.34λ) at a plane (− 0.716 μm). The focal depth is increased upon increasing the slit

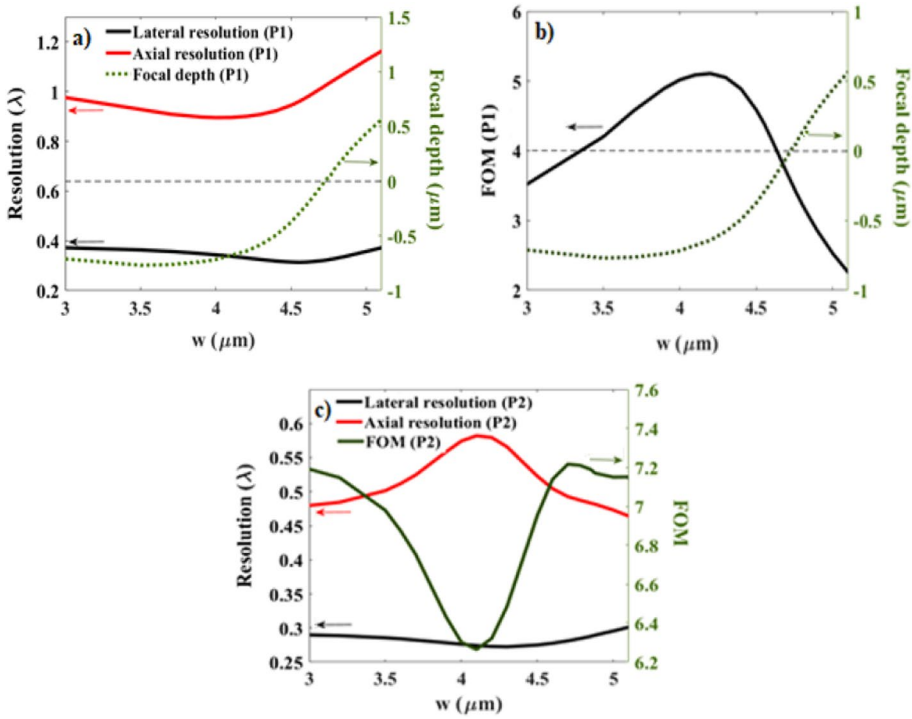

Fig. 5 **a** P1 lateral, axial resolution and the corresponding focal depth with respect to the slit width at fixed thickness (h = 0.4 μm). **b** P1 FOM and the corresponding focal depth with respect to the slit width. **c** P2 lateral, axial resolution and the corresponding FOM with respect to the slit width

width where the focusing point is emerged outside the lens at (w = 4.75 μm) giving rise to a lateral resolution down to (~0.32 λ) and axial resolution down to (~0.89λ). Further increase in focal depth leads to deterioration in resolution particularly in the axial direction. To relate the axial and lateral resolution, a FOM is calculated and presented with the corresponding focal depth as presented in Fig. 5b. The highest FOM (~5.1) is obtained inside the lens at the focal plane (-0.64 μm) for (w = 4.2 μm). After this point, a dramatic decrease in FOM accompanied with a significant enhancement in focusing depth are observed. At P2, an outstanding lateral resolution down to (~0.27λ) accompanied with excellent axial resolution down to (~0.57λ) for w = 4.3 μm is obtained as shown in Fig. 5c. The FOM exhibits its maximum (~7.2) for (w = 4.7 μm) in correspondence to lateral and axial resolution down to (~0.28λ) and (~0.49λ), respectively.

Noteworthy, the proposed lens performance, with slit parameters h = 0.4 μm and w = 4.8 μm, is examined along different wavelengths within the bandgap as demonstrated in Fig. 6a–d. It may be seen that the lens preserves the focusing at P1 with less resolution limit. However, a great advantage of increasing the focal depth is obtained upon decreasing the wavelength with attainable sub-diffraction limit in lateral direction. Remarkably, the wavelength of 2.6 μm allows lateral focusing resolution down to (~0.46λ) at a focal depth up to 1.766 μm. On the other hand, upon increasing the wavelength, the axial resolution is increased down to (~0.86λ) at λ = 3.6 μm. However, such increase is achieved at the cost of the focal depth that the focusing point is incorporated within the slit by a distance

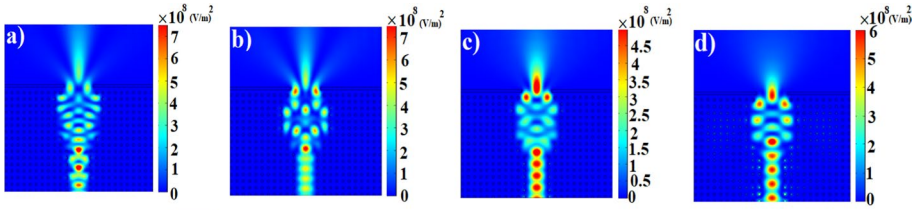

Fig. 6 The electric field intensity distribution at different wavelengths within the band gap region, **a** = 2.6 μm, **b** λ = 2.8 μm, **c** λ = 3.2 μm and **d** λ = 3.6 μm

(−0.553 μm) from the interface at λ = 3.6 μm. Meanwhile, focusing at P2 deteriorates above and below the central bandgap wavelength (3 μm) except for ambiguous focusing at λ = 2.8 μm as shown in Fig. 6b.

Next, the loss sources of the suggested design are discussed thoroughly. At room temperature, the silicon is lossless in the region of IR wavelengths showing a null extinction factor of the refractive index that represents the absorption coefficient with negligible imaginary part of the dielectric constant (κ = 0, $\varepsilon'' = 0$) (Zhang et al. 2006; Sturm and Reaves 1992; Vega et al. 2015). Hence, the loss due to silicon absorption is minimal in our design. In addition, the metallic structures at the exit of the cavity works as reflectors minimizing the losses and inducing enhancement of the image quality. However, the major losses are attributed to the insertion losses and the reflection at the end of the waveguide cavity due to the impedance mismatch between the PhC waveguide mode and the input and output modes (Quynh et al. 2009). The out-of-plane radiation losses of our design is minimal due to the large thickness of the PhC, so that the light cone is far away from the Brillouin-zone edge (Akiki et al. 2020). Other factors influence the losses due to fabrication processes such as the extrinsic losses due to the impurities in the form of free electrons and the shape irregularities leading to scattering losses due to wall roughness. In addition, loss due to the reflectance that is considered as the major source of losses (Joanopoulos 2008). The bulk intrinsic silicon is previously proven to exhibit normalized reflection of ~ 30% (Vega et al. 2015). For our proposed cavity design, we ensure high electric field confinement and minimal leakage of the propagating mode into the PhC by using a sufficient number of silicon rods on both sides of the guiding cavity (Joanopoulos 2008), 11 silicon rods on each side. It should be noted that the infrared signals are usually transported through the PhC structures that have a power level of micro-watt when the input signal from a semiconductor laser is on the power level of melli-watt (Wang et al. 2013). Owing to the low power effect, the biological samples undergo no damaging effect. The normalized transmission power is investigated along the bandgap region from 2.4 to 3.6 μm as shown in Fig. 7. From the figure, several dips are observed along the transmission spectrum representing the resonating modes diminishing the focusing behavior, a phenomenon out of focus of this study. Meanwhile, high transmission power is exhibited along the spectrum, avoided the resonating modes, demonstrating small loses. The transmitted power data of the investigated focusing behavior at different wavelengths along with their focusing behavior are presented in Table1.

The suggested design has rods of diameter of 0.2 μm that are arranged with a square lattice of pitch of 1 μm. It should be noted that photonic crystal slab with small diameter of 0.2 μm and minimum spacing of 1.74 μm have been fabricated in Liyong et al. (2012). Therefore, it is believed that the suggested design can be fabricated successfully. The design can be fabricated using different techniques such as nano-imprint (Chen and

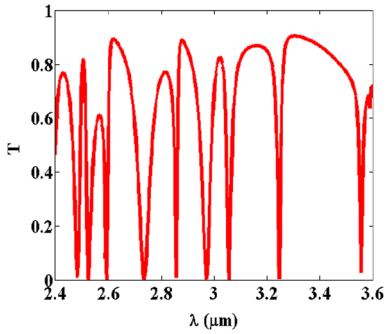

Fig. 7 The transmitted power along the bandgap wavelength range

Table 1 Ssummary of focusing effect in lateral and axial direction, the corresponding FOM and focal depth and the corresponding normalized transmission power with respect to different propagating wavelengths

Operating wavelength (μm)	Lateral resolution	Axial resolution	FOM	Focal depth (μm)	Transmitted power [dB]
2.6	0.46 λ	2.93λ	0.75	1.766	−0.637
2.8	0.34 λ	1.44λ	2.05	1.031	−1.216
3	0.32λ	0.89λ	3.51	0.133	−1.565
3.2	0.41 λ	1.03λ	2.35	0.249	−0.718
3.6	0.43 λ	0.85λ	2.71	−0.553	−1.431

Sun 2010), holographic or electron beam lithography (EBL) inductively coupled plasma etching and reactive ion etching techniques (Liyong et al. 2012; Meng et al. 2011). However, the EBL has the advantage of high resolution and being a mask less technique where the substrate is directly written upon like a pen (Fransisc 2008). To fabricate the proposed design, a silicon-on-insulator wafer with sufficient high thickness of silicon is used. On top of the wafer surface, ma-N2401 resist is spin coated, then EBL directly write the PhC pattern onto it. Finally, the inductively coupled plasma (ICP) etching technique is conducted using a SF6 plasma at 500 W ICP power and 20 mT pressure to transfer the pattern into the top silicon layer (Fransisc 2008). The fabrication process is demonstrated in Fig. 8.

The optimized data obtained are summarized demonstrating the optimum performance of each functionality, lateral resolution, axial resolution, focal depth and FOM, along with recently data obtained in previous studies as presented in Table 2. From the table, the highest lateral resolution obtained is down to ~ 0.27λ which is slightly less than that previously

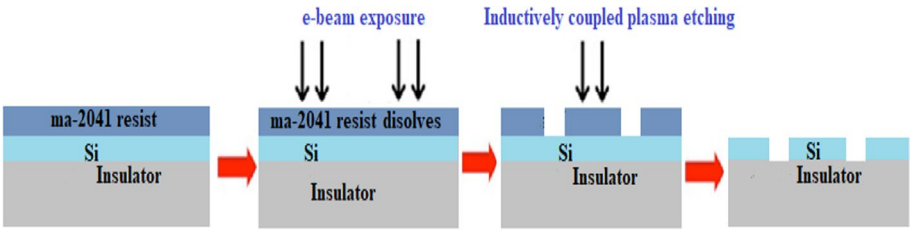

Fig. 8 Flow chart demonstrating the steps of e-beam nanolithography fabrication process

Table 2 Summary of the optimized functionalities including maximum lateral, axial resolution, FOM and maximum focal depth in correspondence to the supporting design and its parameters

Optimized Functionality	λ (μm)	The design	Ag Slit parameters	Lateral resolution	Axial resolution	FOM	Focal depth (μm)	Previous studies
Max lateral resolution	3	PhC/Ag rods/ Ag slit	h = 0.4(μm) w = 4.3(μm)	**0.27λ**	0.57λ	6.48	P2	**#0.19λ** (Salama et al. 2020), **#0.17λ** (Huang, et al. 2019)
Max Axial resolution	3	PhC/Ag rods/ Ag	h = 2(μm) w = 5(μm)	0.33λ	**0.42λ**	7.33	P2	**0.41λ** Lee et al. (2019)
Max FOM	3	PhC/Ag rods	h = 0	0.31 λ	0.43λ	**7.80**	P2	–
Max focal depth	3	PhC	–	0.72λ	–	–	**4.16**	**–**
Max focal depth with sub-diffraction lateral resolution	3	PhC/Ag rods	–	0.47λ	1.61λ	1.32	**0.984**	**# 133 μm** (Bayati et al. 2020) **#Far field imaging with a lateral resolution of 0.17λ**(Huang et al. 2019)
Max focal depth with sub-diffraction lateral resolution	2.6	PhC/Ag rods/ Ag slit	h = 0.4(μm) w = 4.8(μm)	0.46λ	2.93λ	0.75	**1.766**	**–**

The bold highlighted cells represent the optimized performance

obtained using HMM that is down to 0.19λ in MID-IR excluding axial confinement (Salama et al. 2020). The highest axial resolution is down to ~ 0.42λ which is comparable to the recent study using silicon rods metasurfaces that operates at visible spectrum (Lee et al. 2019). Moreover, the focusing depths of the outer focusing point (P1) are also demonstrated. Remarkably, the focal depth could be enhanced either by simultaneous decreasing the slit thickness (h) and increasing the slit width (w) or by removing the slit. Removing the slit allows a focal depth up to 0.984 μm at a wavelength of 3 μm with axial confinement above the diffraction limit. In addition, the smaller operating wavelengths than 3 μm shows a high focal depth of the PhC/Ag rods/ Ag slit structure as can be observed at operating wavelength of λ = 2.6 μm where the focal depth reaches ~ 1.766 μm. Previous studies demonstrate high focal depths, up to 133 μm (Bayati et al. 2020), and far field imaging sacrificing the axial light confinement (Huang et al. 2019). To the best of our knowledge, it is the first study that provides multiple functionalities of simultaneous sub-diffraction lateral and axial resolution, and focal depth using a single platform. These functionalities are crucial for three dimensional (3D) imaging beating the abbe diffraction limit in both directions with significant enhancement of FOM from 2 for conventional optics to FOM of ~ 8 for our design. Moreover, our design has shown advanced applicability and simplicity compared with other high FOM techniques such as the scanning microscopy and the generating structured interference at a focal spot through providing a single platform for 3D imaging. Furthermore, imaging in IR-region is of pivotal importance for examining the sub-cellular components as it provides fingerprints for the structural information in a label free manner. In addition, the proposed design requires a working power level in micro-watt and hence, no photo-damage effect is encountered upon irradiance. We expect that our design will have a tremendous impact on imaging area particularly in digital optics and holography as useful technique for 3D imaging for biomedical applications.

4 Conclusion

In summary, we have introduced a novel metalens design based on Si PhC with silver rods and slit. The sub-diffraction resolution in both lateral and axial dimensions which are the detrimental parameters of the PSF are addressed. The proposed lens provides a number of focusing points with variant resolution limits. The lens shows maximum lateral resolution down to (~ 0.27λ) with corresponding axial resolution down to (~ 0.47λ) at focusing P2 at λ = 3 μm which greatly beating the diffraction limit of PSF in both directions. Moreover, the focusing depths of the outer focusing point (P1) are also demonstrated. Remarkably, the focal depth could be enhanced either by simultaneous decreasing the slit thickness (h) and increasing the slit width (w) or by reducing the propagating wavelength. The highest focal depth obtained is up to 1.766 μm at λ = 2.6 μm.

5 Materials and methods

Finite element method (COMSOL Multiphysics software) has been used for simulating the optical response of the proposed structures to the propagating waves.

Author contributions SO has suggested the concept and supervised the project. NS has performed the final design, theoretical modelling, numerical simulations and written the manuscript. SA has contributed to the technical discussion regarding the biomedical imaging requirements. MH has helped understanding the modeling technique of the photonic crystal. MS has contributed to the technical discussion regarding

meta-lens physical concepts and related design issues presented in the paper. All the authors have revised and edited the manuscript.

Funding Open access funding provided by The Science, Technology & Innovation Funding Authority (STDF) in cooperation with The Egyptian Knowledge Bank (EKB). The authors declare that no funds, grants, or other support were received during the preparation of this manuscript.

Declarations

Conflict of interest The authors declare no competing interest.

Open Access This article is licensed under a Creative Commons Attribution 4.0 International License, which permits use, sharing, adaptation, distribution and reproduction in any medium or format, as long as you give appropriate credit to the original author(s) and the source, provide a link to the Creative Commons licence, and indicate if changes were made. The images or other third party material in this article are included in the article's Creative Commons licence, unless indicated otherwise in a credit line to the material. If material is not included in the article's Creative Commons licence and your intended use is not permitted by statutory regulation or exceeds the permitted use, you will need to obtain permission directly from the copyright holder. To view a copy of this licence, visit http://creativecommons.org/licenses/by/4.0/.

References

Abbasi, A., et al.: Ultra compact and fast all optical flip flop design in photonic crystal platform. Opt. Commun. **285**(24), 5073–5078 (2012). https://doi.org/10.1016/j.optcom.2012.06.095

Aieta, F., et al.: Aberration-free ultrathin flat lenses and axicons at telecom wavelengths based on plasmonic metasurfaces. Nano Lett. **12**(9), 4932–4936 (2012)

Akiki, E., et al.: High-Q THz photonic crystal cavity on a low-loss suspended silicon platform. IEEE Trans. Terahertz Sci. Technol. **11**(1), 42–53 (2021). https://doi.org/10.1109/TTHZ.2020.3019928

Areed, N.F., Hussien, M., Obayya, S.S.: Reconfigurable coupler-based metallic photonic crystal lens and nematic liquid crystal. J. Opt. Soc. Am. B **35**, 2459–2466 (2018)

Bailey, B., Farkas, D., Taylor, D., et al.: Enhancement of axial resolution in fluorescence microscopy by standing-wave excitation. Nature **366**, 44–48 (1993)

Banaei, A., et al.: Band gap properties of two-dimensional photonic crystal structures with rectangular lattice. J. Opt. Commun. **36**(2), 109–114 (2015)

Bayati, E., et al.: Inverse designed metalenses with extended depth of focus. ACS Photon. **7**(4), 873–878 (2020)

Berry, M.V., Balazs, N.L.: Nonspreading wave packets. Am. J. Phys. **47**(3), 264–267 (1979). https://doi.org/10.1119/1.11855

Carr, G.L.: Resolution limits for infrared microspectroscopy explored with synchrotron radiation. Rev. Sci. Instrum. **72**(3), 1613–1619 (2001)

Chen, J.Y., Sun, K.W.: Enhancement of the light conversion efficiency of silicon solar cells by using nanoimprint anti-reflection layer. Sol. En. Mat. Sol. Cells **94**, 629–633 (2010)

Cui, T., Qi, M., Wan, X., et al.: Coding metamaterials, digital metamaterials and programmable metamaterials. Light. Sci. Appl. **3**, 1–9, e218 (2014)

Fan, X., et al.: Axially tailored light field by means of a dielectric metalens. Phys. Rev. Appl. **14**(2), 024035 (2020)

Fransisc, P.M.: Electron beam liohtography for nanofabrication. Institute de Microelectrònica de Barcelona (2008)

Gustafsson, M.G., et al.: I5M: 3D widefield light microscopy with better than 100 nm axial resolution. J. Microsc. **195**, 10–16 (1999)

Haddadan, F., Soroosh, M., Alaei-Sheini, N.: Designing an electro-optical encoder based on photonic crystals using the graphene–Al_2O_3 stacks. Appl. Opt. **59**, 2179–2185 (2020)

Hell, S., et al.: Measurement of the 4Pi-confocal point spread function proves 75 nm axial resolution. Appl. Phys. Lett. **64**(11), 1335–1337 (1994)

https://www.comsol.com/comsol-multiphysics.

Huang, T. et al.: Far-field subwavelength resolution imaging by encoding spatial harmonics into spoof surface plasmon polaritons. arXiv: Optics n. pag. (2019)

Jacob, Z., Alekseyev, L.V., Narimanov, L.V.: Optical hyperlens: far-field imaging beyond the diffraction limit. Opt. Express **14**, 8247–8256 (2006)

Jin Hou, D.S., et al.: Slab-thickness dependence of photonic bandgap in photonic-crystal slabs. IEEE J. Select. Top. Quantum Electron. **18**(6), 1636–1642 (2012). https://doi.org/10.1109/JSTQE.2011.2169773

Joanopoulos, J.D.: Photonic Crystals Modeling the Flow of Light. Princeton University Press, Princeton (2008)

Johnson, S.G., Joannopoulos, J.D.: Block-iterative frequency-domain methods for Maxwell's equations in a planewave basis. Opt. Express **8**, 173–190 (2001)

Kihm, K. D.: Confocal laser scanning microscopy (CLSM). In: Near-Field Characterization of Micro/Nano-Scaled Fluid Flows, Experimental Fluid Mechanics, vol. 0, Springer, Berlin, Heidelberg (2011)

Lee, D., et al.: All-dielectric metasurface imaging platform applicable to laser scanning microscopy with enhanced axial resolution and wavelength selection. Opt. Mater. Express **9**(8), 3248–3259 (2019)

Li, Z.-Y., Wang, C., Lin, G.: Silicon photonic crystals towards optical integration. In: Passaro, V. (ed.) Advances in Photonic Crystals. InTech, Vandavasi (2013)

Liyong, J., et al.: Design and fabrication of rod-type two-dimensional photonic crystal slabs with large high-order bandgaps in near-infrared wavelengths. Opt. Lett. **37**, 1424–1426 (2012)

Mahmoud, S.S., et al.: Highly sensitive photonic crystal gamma ray dosimeter. Opt. Quantum Electron, 348–1–348–19 (2021). https://doi.org/10.1007/s11082-021-02968-y

Maleki, M.J., Soroosh, M.: A novel proposal for performance improvement in two-dimensional photonic crystal-based 2-to-4 decoders. Laser Phys. **30**(7), 076203–1–076203–6 (2020). https://doi.org/10.1088/1555-6611/ab9089

Maleki, M.J., Soroosh, M.: Design and simulation of a compact all-optical 2-to-1 digital multiplexer based on photonic crystal resonant cavity. Opt. Quant. Electron. **54**, 1458–1473 (2022)

Maleki, M.J., Soroosh, M., Mir, A.: Improving the performance of 2-to-4 optical decoders based on photonic crystal structures. Crystals **9**, 635-1–635-9 (2019b)

Maleki, M.J., et al.: Designing an ultra-fast all-optical full-adder based on nonlinear photonic crystal cavities. Opt. Quantum Electron. **52**(4), 1–11 (2020)

Maleki, M.J., Soroosh, M., Mir, A.: Ultra-fast all-optical 2-to-4 decoder based on a photonic crystal structure. Appl. Opt. **59**, 5422–5428 (2020)

Mehdizadeh, F., Soroosh, M., Alipour-Banaei, H., Farshidi, E.: All optical 2-bit analog to digital converter using photonic crystal based cavities. Opt. Quant. Electron. **49**, 38-1–38-11 (2017)

Meng, X. et al.: Design and fabrication of photonic crystals in epitaxy-free silicon for ultrathin solar cells. In Asia Communications and Photonics Conference and Exhibition, Shanghai, China. pp. 831207-831207-7 (2011)

Miller, L.M., Dumas, P.: Chemical imaging of biological tissue with synchrotron infrared light. Biochim. Biophys. Acta (BBA) – Biomembr. **1758**(7), 846–857 (2006). https://doi.org/10.1016/j.bbamem.2006.04.010

Mohammadi, B., Soroosh, M., Kovsarian, A., et al.: Improving the transmission efficiency in eight-channel all optical demultiplexers. Photon. Netw. Commun. **38**, 115–120 (2019)

Mohammadi, M., Habibi, F., Seifouri, M., et al.: Recent advances on all-optical photonic crystal analog-to-digital converter (ADC). Opt. Quantum Electron. **54**, 1–22 (2022)

Notomi, M., et al.: On-chip all-optical switching and memory by silicon photonic crystal nanocavities. Adv. Opt. Technol. **2008**, 1–10 (2008). https://doi.org/10.1155/2008/568936

Padilla, W.J., Averitt, R.D.: Imaging with metamaterials. Nat. Rev. Phys. **4**, 85–100 (2022)

Pan, W., et al.: A terahertz demultiplexer based on metamaterials applied to terahertz communication systems. Progr. Electromagn. Res. Lett. **97**, 13–19 (2021). https://doi.org/10.2528/PIERL21011902

Parandin, F., Malmir, M.R.: Reconfigurable all optical half adder and optical XOR and AND logic gates based on 2D photonic crystals. Opt. Quant. Electron. **52**, 56-1–56-80 (2020)

Rayleigh, L.F.R.S.: XXXI Investigations in optics, with special reference to the spectroscope. Lond. Edinburgh Dublin Philos. Mag. J. Sci. **8**, 261–274 (1879)

Ren, Y.-X., et al.: Non-diffracting light wave: fundamentals and biomedical applications. Front. Phys. **9**, 698343-1–698343-30 (2021)

Salama, N., Desouky, M., Swillam, M.: Sub-wavelength focusing in air using semiconductor based hyperbolic metamaterial for infrared imaging. In Frontiers in Optics, Optical Society of America (2018)

Salama, N.A., et al.: Free space super focusing using all dielectric hyperbolic metamaterial. Sci. Rep. **10**(1), 1–9 (2020)

Salama, N., Desouky, M., Swillam, M.: Hypergrating for sub-diffractional focusing enhancement in air in the mid-IR wavelength range. In High Contrast Metastructures VIII. Vol. 10928, International Society for Optics and Photonics (2019)

Sandeau, N., Giovannini, H.: Increasing the lateral resolution of 4Pi fluorescence microscopes. J. Opt. Soc. Am. A **23**, 1089–1095 (2006)

Shaari, S., Azliza, J.A.: Photonic crystal multiplexer/demultiplexer device for optical communications. In Frontiers in Guided Wave Optics and Optoelectronics. IntechOpen, 2010.
Shankar, R., et al.: Mid-infrared photonic crystal cavities in silicon. Opt. Express **19**(6), 5579–5586 (2011)
Shinya, A., et al.: All-optical flip-flop circuit composed of coupled two-port resonant tunneling filter in two-dimensional photonic crystal slab. Opt. Express **14**(3), 1230–1235 (2006)
Silien, C., et al.: A framework for far-field infrared absorption microscopy beyond the diffraction limit. Opt. Express **20**(28), 29694–29704 (2012)
Sturm, J.C., Reaves, C.M.: Silicon temperature measurement by infrared absorption. Fundamental processes and doping effects. IEEE Trans. Electron. Devices **39**(1), 81–88 (1992). https://doi.org/10.1109/16.108215
Tran, Q.V., et al.: Photonic crystal membrane waveguides with low insertion losses. Appl. Phys. Lett. **95**(6), 061105-1–061105-8 (2009). https://doi.org/10.1063/1.3205452
Vega, D. et al.: The effect of absorption losses on the optical behaviour of macroporous silicon photonic crystal selective filters. J. Lightw. Technol. (2015)
Willig, K., Rizzoli, S., Westphal, V., et al.: STED microscopy reveals that synaptotagmin remains clustered after synaptic vesicle exocytosis. Nature **440**(7086), 935–939 (2006)
Yang, X., Xie, H., Alonas, E., et al.: Mirror-enhanced super-resolution microscopy. Light. Sci. Appl. **5**, 1–8 (2016)
Zamanian-Dehkordi, S.S., Soroosh, M., Akbarizadeh, G.: An ultra-fast all-optical RS flip-flop based on nonlinear photonic crystal structures. Opt. Rev. **25**, 523–531 (2018)
Zhang, X., John, S.: Photonic crystal light trapping for photocatalysis. Opt. Express **29**, 22376–22402 (2021)
Zhang, Y., Li, Z., Li, B.: Multimode interference effect and self-imaging principle in two-dimensional silicon photonic crystal waveguides for terahertz waves. Opt. Express **14**(7), 2679–2689 (2006). https://doi.org/10.1364/OE.14.002679
Zheng, X., et al.: A tunable 1x4 silicon CMOS photonic wavelength multiplexer/demultiplexer for dense optical interconnects. Opt. Express **18**, 5151–5160 (2010)
Zhuo, Y., Cunningham, B.: Label-free biosensor imaging on photonic crystal surfaces. Sensors **15**(9), 21613–21635 (2015). https://doi.org/10.3390/s150921613

Publisher's Note Springer Nature remains neutral with regard to jurisdictional claims in published maps and institutional affiliations.

Authors and Affiliations

Norhan A. Salama[1,3] · Mohamed A. Swillam[2] · Mohamed Farhat O. Hameed[3,4,5] · Y. Badr[6] · Shaimaa M. Alexeree[1] · Salah S. A. Obayya[3,7]

1 Department of Laser Applications in Metrology, Photochemistry and Agriculture, National Institute of Laser Enhanced Sciences, Cairo University, Giza, Egypt

2 Department of Physics, The American University in Cairo, Cairo 11835, Egypt

3 Centre for Photonics and Smart Materials, Zewail City of Science, Technology and Innovation, October Gardens, 6th of October City, Giza 12578, Egypt

4 Nanotechnology and Nanoelectronics Engineering Program, Zewail City of Science, Technology and Innovation, October Gardens, 6th of October City, Giza 12578, Egypt

5 Mathematics and Engineering Physics Department, Faculty of Engineering, University of Mansoura, Mansoura 35516, Egypt

6 Department of Laser Sciences and Interactions, National Institute of Laser Enhanced Sciences, Cairo University, Giza 12613, Egypt

7 Department of Electronics and Communications Engineering, Faculty of Engineering, University of Mansoura, Mansoura 35516, Egypt